

Simulation and modelling of convective mixing of carbon dioxide in geological formations

Marco De Paoli^{1,2}, Francesco Zonta³, Lea Enzenberger², Eliza Coliban², and Sergio Pirozzoli⁴

¹Physics of Fluids Group and Max Planck Center for Complex Fluid Dynamics and J. M. Burgers Centre for Fluid Dynamics, University of Twente, P.O. Box 217, 7500AE Enschede, The Netherlands

²Institute of Fluid Mechanics and Heat Transfer, TU Wien, 1060 Vienna, Austria

³School of Engineering, Newcastle University, Newcastle upon Tyne NE1 7RU, United Kingdom

⁴Dipartimento di Ingegneria Meccanica e Aerospaziale, Sapienza Università di Roma, 00184 Rome, Italy

Key Points:

- Convective mixing of carbon dioxide in geological formations follows different regimes
- During a regime in which the flux is constant, mixing in 3D simulations is 13% larger than in 2D simulations, well below previous estimates
- A simple model can be employed to accurately reproduce the flow evolution for all the regimes and all the Rayleigh-Darcy numbers

arXiv:2501.06090v1 [physics.flu-dyn] 10 Jan 2025

Corresponding author: Marco De Paoli, m.depaoli@utwente.nl, marco.de.paoli@tuwien.ac.at

Abstract

We perform large-scale numerical simulations of convection in 3D porous media at Rayleigh-Darcy numbers up to $Ra = 8 \times 10^4$. To investigate convective mixing of carbon dioxide (CO_2) in geological formations, we consider a semi-infinite domain, where the CO_2 concentration is constant at top and no flux is prescribed at bottom. Convection begins with a diffusion-dominated phase, transitions to convection-driven solute finger formation, and ends with a shutdown stage as fingers reach the bottom boundary and the concentration in the system increases. For $Ra \geq 5 \times 10^3$, we observe a constant flux regime with dissolution flux stabilizing at 0.019, approximately 13% higher than in 2D estimates. At high Ra , the top boundary exhibits hierarchical flow structures that drive the formation of large megaplumes in the interior, consistent with Rayleigh-Darcy convection. These findings extend solutal convection insights to 3D and high- Ra , improving the reliability of models predicting the long-term CO_2 dynamics in the subsurface.

Plain Language Summary

Geological sequestration of carbon dioxide (CO_2) consists of injecting large amounts of CO_2 in underground formations with the aim of permanent storage. This process is key to reduce emissions of greenhouse gases in the atmosphere and to support energy transition. After injection, CO_2 combines with the resident fluid (brine) and remains stably trapped in the formation preventing leakages to the atmosphere. The mixing process of CO_2 and brine may take place over hundred or thousand of years, and originates density-driven flows that in turn influence mixing. Predicting the evolution of this process is crucial to design injection strategies. Field and laboratory measurements are challenging due to the inaccessibility of the underground sites and the time-scale of the flow processes. Here we employ massive numerical simulations to predict the underground CO_2 dynamics, which depends on the fluid properties, on the rock properties and on the morphology of the formation. We systematically investigate the flow dynamics in three-dimensional systems, and provide a robust quantification of the differences occurring with respect to ideal two-dimensional systems. Finally, we derive a simple, reliable and accurate physical model to predict, design and control the post-injection dynamics of CO_2 .

1 Introduction

Natural convection takes place when a flow is driven by the density differences existing within the fluid domain. Convective flows occurring within a porous medium and characterized by density variations induced by heat or solute, are particularly relevant to geophysical processes. The formation of sea ice, for instance, is controlled by a convective flow (Worster, 2019), driven by the salt- and temperature-induced density variations, and it occurs within a newly formed and porous icy matrix, defined mushy layer (Feltham, 2006; Worster, 2019; Wells et al., 2019). In dry salt lakes, subsurface convective processes are responsible for the vertical transport of salt, a fundamental mechanism in arid regions, leaving superficial polygonally-shaped crusts as signature (Lasser et al., 2021, 2023). Recently, the problem of convection in porous media has become pivotal to address the challenge of carbon dioxide (CO_2) sequestration (Huppert & Neufeld, 2014), a key process required to drive the energy transition.

With the aim of permanent storage, supercritical CO_2 is injected in underground geological formations (e.g., saline aquifers), which may be idealized as porous regions filled with brine and confined by two low-permeability layers, acting as hydrodynamics barriers to the flow (Neufeld et al., 2010; De Paoli, 2021). In these conditions, supercritical CO_2 is lighter than the resident fluid, and after injection it accumulates underneath the upper confining layer (Emami-Meybodi et al., 2015). This situation is potentially critical, as a fracture of this natural barrier may allow CO_2 to escape to the upper geological layers and eventually to the atmosphere. However, CO_2 is partially miscible and brine, and the resulting mixture

(CO₂+brine) is heavier than both starting fluids. The process of accumulation of this heavy mixture at the upper layer is key, as it promotes the formation of flow instabilities (called plumes or fingers) that, due to convection, increase the mixing rate of CO₂ in brine (Ennis-King et al., 2005; Xu et al., 2006) and reduce the risk of leakage. Therefore, predicting the mixing rate as a function of the fluid properties, rock properties and formation morphology is key to accurately address the process of geological carbon sequestration (Ulloa & Letelier, 2022; Letelier et al., 2023).

The dynamics of the CO₂-brine mixing process is characterized by three main phases (Slim et al., 2013; Slim, 2014): i) initially, solute transport is limited to the fluid-fluid interface, and it is controlled by diffusion; ii) then, when the dense, CO₂-rich fluid layer becomes sufficiently thick, it becomes unstable and promotes the formation of small fingers; iii) these fingers grow vertically and eventually merge with neighboring plumes generating larger and persistent structures in a statistically-steady fashion; iv) finally, when the domain is saturated with the CO₂-rich fluid carried downward by the megaplumes, the mixing of CO₂ slows progressively down (Hewitt et al., 2013). The single dimensionless governing parameter is the Rayleigh-Darcy number Ra , which expresses the ratio of the strength of driving (buoyancy) to dissipative (viscosity and molecular diffusion) mechanisms. It contains the fluids, medium and formation properties, and it may span over few decades, namely from $O(10)$ (Emami-Meybodi, 2017) to $O(10^5)$ (Hu et al., 2023). Despite the highly non-linear and transient character described, this system has been accurately characterized numerically in two-dimensions (Emami-Meybodi et al., 2015; Hewitt, 2020; De Paoli, 2023). The three-dimensional problem, in contrast, is still partially unexplored, due to the huge computational cost required to accurately resolve the flow at large Ra . With the exception of few works at moderate Ra (Liyanaage et al., 2024; Imuetinyan et al., 2024; Sin et al., 2024), the opacity of the media represents an intrinsic limitation for the laboratory experiments, preventing from obtaining simultaneous measurements of flow and solute. In this work, we aim precisely at this gap.

We perform high-resolution, large-scale simulations of solute convection in two-dimensional and three-dimensional porous media at unprecedented Rayleigh-Darcy numbers, namely up to $Ra = 8 \times 10^4$. Exploiting this unique database, which we make freely available (De Paoli et al., 2025), we provide a thorough characterization of the flow dynamics. We analyze the flow in terms of dissolution rate of solute and flow structures near the fluid-fluid interface. First, we confirm that in two-dimensional systems the dissolution rate during the constant flux regime (phase iii described above) agrees with previous findings (Hesse, 2008; Hewitt et al., 2013; Slim, 2014; De Paoli et al., 2017; Wen, Akhbari, et al., 2018). Then we extend our simulations to 3D flows, and we identify a remarkable difference with respect to previous works (Pau et al., 2010), suggesting that in 3D the dissolution rate is not 25% larger than in 2D, but only 13%. Finally, we present a physical model that accurately captures the mixing dynamics, and can be used to design, predict and control the CO₂ post-injection dynamics.

2 Methodology

2.1 Problem formulation

We consider homogeneous, isotropic and fluid-saturated porous media characterized by permeability κ and porosity ϕ . We indicate with x^* , z^* the horizontal directions and with y^* the vertical direction, perpendicular to the horizontal boundaries and aligned with gravity \mathbf{g} (see Figs. 1a-i,a-ii). Assuming the validity of the Boussinesq approximation (Landman & Schotting, 2007; Zonta & Soldati, 2018), the flow is incompressible and described by the continuity and the Darcy equations:

$$\nabla^* \cdot \mathbf{u}^* = 0 \quad , \quad \mathbf{u}^* = -\frac{\kappa}{\mu} (\nabla^* P^* + \rho^* g \mathbf{j}) \quad , \quad (1)$$

with μ the fluid viscosity (constant), $\mathbf{u}^* = (u^*, v^*, w^*)$ the volume-averaged velocity field, P^* the pressure, and \mathbf{j} the vertical unit vector (* indicates dimensional quantities). The flow

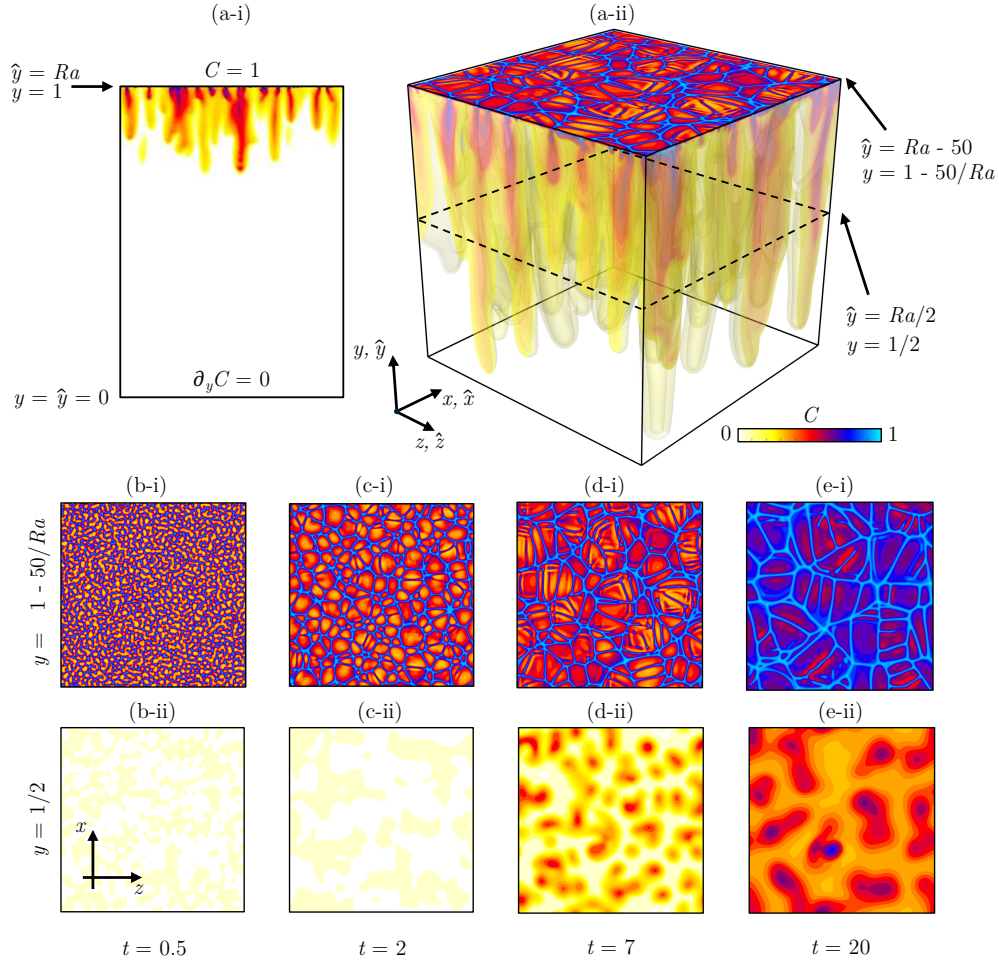


Figure 1. Flow configuration (simulation B6, $Ra = 5 \times 10^3$, see Tab. S1). (a-i) Concentration field at time $t = 2.0$, with indication of the boundary conditions and location of the domain wall (convective - y - and diffusive - \hat{y} - units, see Sec. 2.2). (a-ii) Concentration distribution at $t = 7$. (b-e) Concentration distribution over horizontal x, z planes located at $y = 1 - 50/Ra$ (or $\hat{y} = Ra - 50$, panels i) and $y = 1/2$ (or $\hat{y} = Ra/2$, panels ii), at different times (indicated below panels ii).

is driven by variations of the fluid density, ρ^* , induced by the presence of a solute (CO_2) that is quantified by the concentration field C^* , with $0 \leq C^* \leq C_{\max}^*$. We consider the density to be a linear function of the solute concentration:

$$\rho^*(C^*) = \rho^*(0) + \Delta\rho^* \frac{C^*}{C_{\max}^*}, \quad (2)$$

with $\Delta\rho^* = \rho^*(C_{\max}^*) - \rho^*(0)$. The concentration field evolves according to the advection-diffusion equation (Nield & Bejan, 2017)

$$\phi \frac{\partial C^*}{\partial t^*} + \nabla^* \cdot (\mathbf{u}^* C^* - \phi D \nabla^* C^*) = 0, \quad (3)$$

where t^* is time and D is the solute diffusivity (considered constant).

The walls are impermeable to the fluid, at the upper boundary the concentration is $C^*(y^* = H^*) = C_{\max}^*$, while at the lower boundary a no-flux condition is applied. The fluid is considered initially still and depleted of solute. Additional numerical details on the initial condition are provided in Text S1.

2.2 Dimensionless equations

Natural flow scales for the convective system considered here are the buoyancy velocity, $\mathcal{U}^* = g\Delta\rho^* \kappa / \mu$, and the domain height, H^* . Employing the set of dimensionless variables:

$$C = \frac{C^*}{C_{\max}^*}, \quad x = \frac{x^*}{H^*}, \quad \mathbf{u} = \frac{\mathbf{u}^*}{\mathcal{U}^*}, \quad (4)$$

$$t = \frac{t^*}{\phi H^* / \mathcal{U}^*}, \quad p = \frac{p^*}{\Delta\rho^* g H^*}, \quad (5)$$

and using the reduced pressure defined as $p^* = P^* + \rho^*(0)gy^*$, the dimensionless form of the governing Eqs. (1),(3) is:

$$\nabla \cdot \mathbf{u} = 0 \quad , \quad \mathbf{u} = -(\nabla p + C\mathbf{j}), \quad (6)$$

$$\frac{\partial C}{\partial t} + \nabla \cdot \left(\mathbf{u}C - \frac{1}{Ra} \nabla C \right) = 0, \quad (7)$$

where

$$Ra = \frac{g\Delta\rho^* \kappa H^*}{\phi D \mu} = \frac{\mathcal{U}^* H^*}{\phi D} \quad (8)$$

is the Rayleigh-Darcy number (hereinafter indicated as Rayleigh number). The problem is controlled by two dimensionless parameters: Ra and the domain aspect ratios, $L_x = L_x^*/H^*$ and $L_z = L_z^*/H^*$. We considered domains having a squared cross section ($L_x = L_z = L$).

To compare the transient evolution of systems having different Ra , a convenient reference length scale should be independent of the domain height (Fu et al., 2013). Taking as reference length scale the distance over which advection and diffusion balance, defined as $\ell^* = \phi D / \mathcal{U}^*$ (Fu et al., 2013; Slim, 2014), we obtain the dimensionless variables in diffusive units (indicated with $\hat{\cdot}$):

$$\hat{x} = \frac{x^*}{\ell^*}, \quad \hat{t} = \frac{t^*}{\phi \ell^* / \mathcal{U}^*}, \quad \hat{p} = \frac{p^*}{\Delta\rho^* g \ell^*}, \quad (9)$$

and the Rayleigh number can be interpreted as a dimensionless domain height, $Ra = H^* / \ell^*$. Note that the dimensionless form of other quantities in Eqs. (4)-(5) remains unchanged. Both dimensionless form of the flow variables will be employed to discuss the results.

Eqs. (6)-(7) are solved numerically with the aid of a second-order finite-difference in-house solver (Pirozzoli et al., 2021; De Paoli et al., 2022). A description of the code and relevant numerical details is provided in Text S1-S3 of the Supporting Information.

3 Results

In this work, we provide for the first time a systematic comparison of the 2D and 3D dissolution dynamics at unprecedented high Ra , namely $10^2 \leq Ra \leq 8 \times 10^4$. The simulations' details are given in Tab. S2. We present the results in terms mixing, quantified by the solute flux through the top wall (Sec. 3.1) and the cumulative amount of solute dissolved (Sec. 3.2), and we relate the mixing dynamics to the flow structures.

3.1 Flux of solute dissolved

The amount of solute that enters the domain per unit of surface area and time is quantified by the dimensionless flux $\widehat{F}(t)$, defined as:

$$\widehat{F}(t) = \int_{\widehat{A}} \left. \frac{\partial C}{\partial \widehat{y}} \right|_{\widehat{y}=1} d\widehat{A}, \quad (10)$$

where $\widehat{A} = L_x^*/\ell^*$ in 2D and $\widehat{A} = L_x^*L_z^*/(\ell^*)^2$ in 3D. The evolution of this response parameter, representative of the actual dissolution dynamics of the system, is reported as a function of the diffusive time \widehat{t} in Fig. 2(a).

The flow dynamics in 2D and 3D systems is qualitatively similar (see also Fig. S4). As described in previous 2D studies (Slim et al., 2013; Hewitt et al., 2013; Slim, 2014; De Paoli et al., 2017; Wen, Akhbari, et al., 2018), the evolution is characterized by several regimes: (i) the system is first controlled by diffusion, as the initial condition prescribes $\mathbf{u} = 0$; the fluid density at the upper boundary layer increases as a result of the concentration contrast between the bulk of the domain and the boundary value, building up a layer of heavy fluid that eventually becomes unstable (Slim, 2014); (ii) later fingers form (Fig. S4a), the flux grows and fingers merge; (iii) the system attains a statistically-steady state, with large and persistent plumes dominating the bulk of the flow and extending vertically (Fig. S4b); (iv) finally, after the fingers reach the lower boundary, the progressively saturates (Fig. S4c): the concentration contrast between the bulk of the domain and the top boundary value diminishes, and it is increasingly harder for the solute to enter the system. We will analyze the dynamics in regimes (i), (iii) and (iv) in Secs. 3.1.1, 3.1.2 and 3.1.3, respectively.

3.1.1 Diffusive phase

Initially, the flow dynamics is marked by the absence of convection ($\mathbf{u} = 0$). Eq. (7) has a self-similar solution (S1), that combined with Eq. (10) allows to determine the evolution of the flux (Slim, 2014; De Paoli et al., 2017):

$$\widehat{F}_d(\widehat{t}) = \frac{1}{\sqrt{\pi \widehat{t}}}. \quad (11)$$

We observe from Fig. 2(a) that the evolution of the system, both in 2D and in 3D, follows Eq. (11) up to $\widehat{t} \approx 10^3$. After the fingers' formation, the flux grows departing from the diffusive state.

3.1.2 Constant flux phase

An initial flux growth is followed by the continuous merging of newly formed fingers into large descending plumes that are persistent in time and space (see Movie S1 and relative discussion in the Supporting Information). The dynamics of the system is statistically steady, and this phase is labelled as *constant flux regime*. The transition from the diffusive to the constant flux regime occurs approximately for $2 \times 10^3 \leq \widehat{t} \leq \widehat{t}_1$, where $\widehat{t}_1 = 2 \times 10^4$ in 2D and 4×10^4 in 3D, respectively. Predicting the time at which this transition occurs is challenging, as it depends on the amplitude of the initial perturbation applied and the Ra considered (see also Sec. 1). In addition, small Ra simulations (A1-A4 and B1-B5) do not reach the constant flux stage, as the domain rapidly saturates. The dimensionality of the

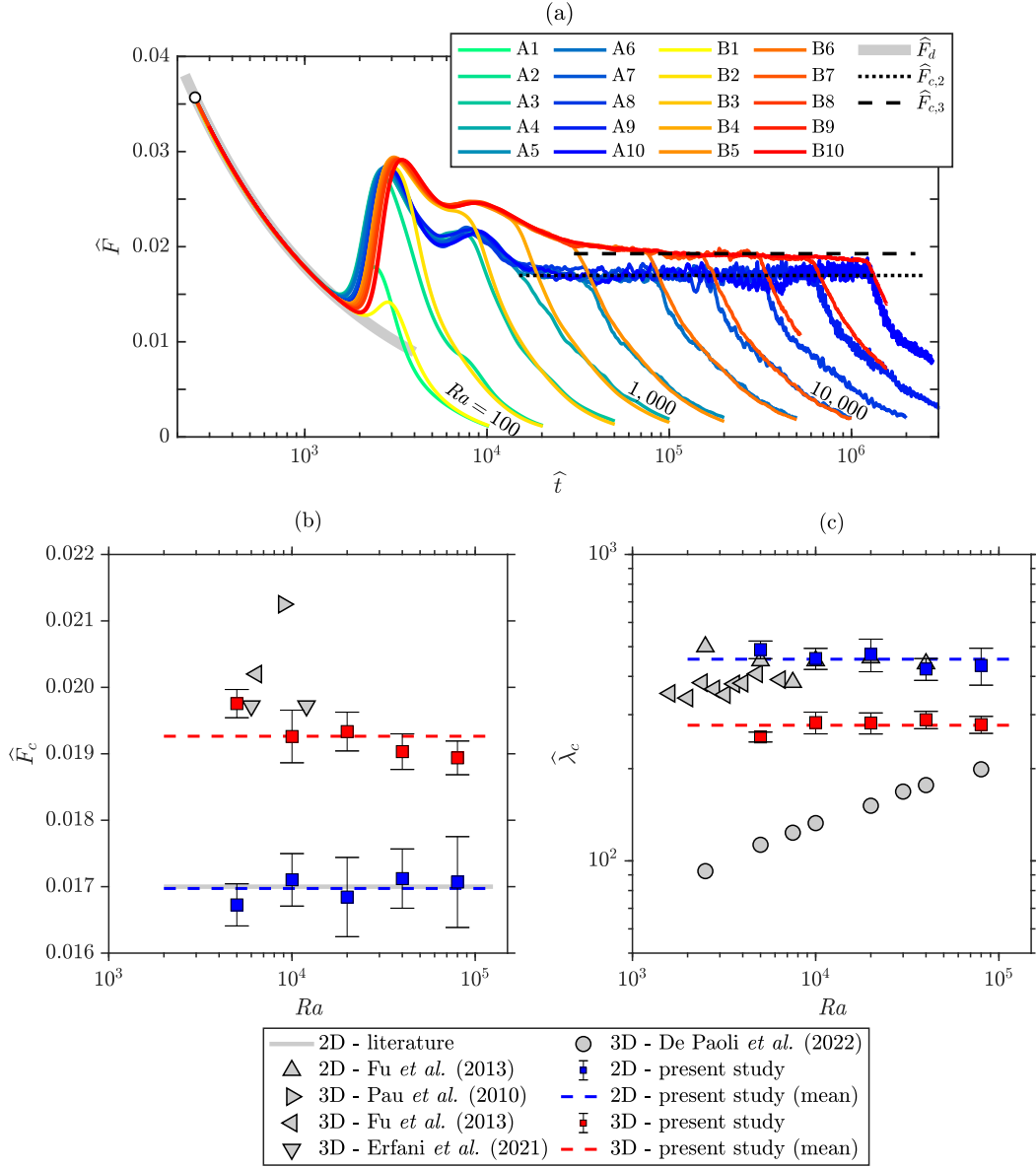


Figure 2. (a) Flux \widehat{F} , defined in (10), obtained in 2D (A#) and 3D (B#) simulations (details in Tab. S2). Results are shown from time $\widehat{t} = 250$ (o) to $\widehat{t} \approx 100 Ra$. The diffusive flux \widehat{F}_d , Eq. (11), and the mean value in the constant flux regime (2D, $\widehat{F}_{c,2}$ in Eq. (12) and 3D, $\widehat{F}_{c,3}$ in Eq. (13)) are also shown. (b) Time-averaged flux during the constant flux regime for $Ra \geq 5 \times 10^3$ (\widehat{F}_c , squares) and corresponding standard deviation ($\sigma(\widehat{F})$, error bar). The ensemble averaged values (dashed lines) are also shown. Results are compared against literature for 2D (see Sec. 3.1.2) and 3D (Pau *et al.*, 2010; Fu *et al.*, 2013; Erfani *et al.*, 2021). (c) Length scales of the flow structures ($\widehat{\lambda}_c$ and corresponding deviation) in the vicinity of the top boundary and averaged during the constant flux regime. Results are compared against measurements by Fu *et al.* (2013) (one-sided) and (De Paoli *et al.*, 2022) (two-sided, Rayleigh-Bénard-Darcy).

system plays also a key role: the process of fingers merging is different in 3D compared to the 2D case, provided the additional degree of freedom available, and for any Ra the flux is larger in 3D than in 2D. This observation is consistent with measurements in Rayleigh-Bénard-Darcy systems, where heat transfer is more efficient in 3D than in 2D (Hewitt et al., 2014; Pirozzoli et al., 2021; Zhu et al., 2024).

An accurate estimate of \widehat{F} during the constant flux regime is essential, as it is employed as a subgrid parameter for large-scale models based on multiphase gravity currents, commonly used to predict the long-term post-injection dynamics (Gasda et al., 2011; MacMinn et al., 2012; MacMinn & Juanes, 2013; Hidalgo et al., 2013; De Paoli, 2021). In the last two decades, several numerical measurements have been provided in 2D, but very few results are available in 3D, also due to the prohibitive computational costs involved. Here we provide for the first time a systematic direct comparison of 2D and 3D flows, and we quantify the dissolution during the constant flux regime at high- Ra .

To determine the mean flux during the constant flux regime, \widehat{F}_c , we only consider the simulations that achieve the constant flux condition, namely simulations A6–A10 in 2D and simulations B6–B10 in 3D (see Fig. 2a). The constant flux regime takes place later in 3D compared to the 2D case. Therefore, we chose different time intervals to determine the time-averaged flux, namely $\widehat{t}_{c,1} \leq \widehat{t} \leq \widehat{t}_{c,2}$ with $\widehat{t}_{c,1} = 2 \times 10^4$ and $\widehat{t}_{c,2} = 16 Ra$ in 2D, and $\widehat{t}_{c,1} = 4 \times 10^4$ and $\widehat{t}_{c,2} = 14 Ra$ in 3D. The upper and lower limits are determined looking at the evolution of \widehat{F} . Note that while the lower limit is constant when defined in diffusive units (\widehat{t}), the upper limit is constant in convective units (t). This is justified by the initial self-similar character of the flow, the behavior of which is independent of the value of Ra until the fingers impact on the lower wall ($t \approx 7 - 8$) (Hewitt et al., 2013; Slim, 2014; De Paoli et al., 2017; Wen, Akhbari, et al., 2018).

We show in Fig. 2(b) the time-averaged values of flux during the constant flux regime, \widehat{F}_c , provided with the standard deviation $\sigma(\widehat{F})$ within the same interval (values listed in Tab. S2). In 2D, present results are in excellent agreement with previous works (Pau et al., 2010; Hesse, 2008; Hewitt et al., 2013; Slim, 2014; De Paoli et al., 2017; Wen, Akhbari, et al., 2018; Erfani et al., 2021; De Paoli et al., 2024) who reported ≈ 0.017 (gray solid line in Fig. 2b). The mean value (\pm deviation) obtained from present simulations is

$$\widehat{F}_{c,2} = 0.01697 \pm 0.00018, \quad (12)$$

which is indicated in Fig. 2(b) by a blue dashed line. Both 0.01697 and 0.0017 fall within the error bars displayed.

In the 3D case, the flux exhibits a weakly decreasing trend, with the constant flux value diminishing from 0.01975 (B6) to 0.01894 (B10), and a mean value

$$\widehat{F}_{c,3} = 0.01926 \pm 0.00032, \quad (13)$$

shown in Fig. 2(b) as a red dashed line. In 3D (see, e.g., simulation B6), the accuracy of Eq. (13) in describing the mean flux is lower than in the 2D case. However, we observe that our results are in agreement with previous findings (Fu et al., 2013; Erfani et al., 2021), with the exception of pioneering work Pau et al. (2010), who reported a flux being 25% larger than in 2D, while in our case we obtain a difference of

$$100 \left(\frac{\widehat{F}_{c,3}}{\widehat{F}_{c,2}} - 1 \right) = 13, 50\%. \quad (14)$$

The implications of these results are considerable, as the findings of Pau et al. (2010) overestimate by a factor ≈ 2 the increased efficiency of the 3D transport mechanisms compared to the 2D ones.

To quantify size and numbers of fingers close to the upper boundary, we compute the power-averaged mean wavenumber k and the corresponding wavelength $\lambda = 1/k$ (De Wit,

2004). Note that this definition of wavelength is also representative of the average cell size, or plume diameter (Fu et al., 2013). In particular, k is obtained as

$$k(t) = \frac{\int_0^{k_N} k_h |\tilde{C}(k^*, t)|^2 dk^*}{\int_0^{k_N} |\tilde{C}(k^*, t)|^2 dk^*}, \quad (15)$$

where k_h is the horizontal wavenumber (Fu et al., 2013; Hewitt et al., 2014, $0 \leq k_h \leq k_N$ with $k_h = k_x$ in 2D, and $k_h = \sqrt{k_x^2 + k_z^2}$ in 3D, and k_N the maximum wavenumber), while $|\tilde{C}|$ is computed by taking the Fourier transform of the concentration field in horizontal direction and is used to obtain the power spectrum density $|\tilde{C}(k^*, t)|^2$. The behavior of k in time (not shown) follows the time-dependent evolution of the dissolution flux. Both in 2D and in 3D, the wavenumber evolves independently of Ra until the system enters the shutdown regime. During the constant flux regime, the wavenumber is also constant. To compare the dynamics at different Ra , the representative structure size expressed in diffusive units, $\hat{\lambda} = Ra/k$, is averaged during the constant flux regime, and we indicate the corresponding value with $\hat{\lambda}_c$. The values relative to each simulation (reported in Tab. S2) indicate that the cell size is larger in 2D than in 3D, and correspond to $\hat{\lambda}_c \approx 455$ and $\hat{\lambda}_c \approx 277$, respectively. During the constant flux regime there is no external length scale controlling the system, and the characteristic scale of the flow is the length over which advection and diffusion balance, ℓ^* . We observe in Fig. 2(c) that $\hat{\lambda}_c \sim Ra^0$ as predicted by Fu et al. (2013). We also observe that present 2D results are in excellent agreement with literature measurements. In 3D, results are still independent of Ra , but have a different value compared to Fu et al. (2013), possibly because their definition of the average cell size is not based on the mean wavenumber, but it is obtained from the number of plumes present in the system. The scaling $\hat{\lambda}_c \sim Ra^0$ is observed both in 2D and 3D flows, and we can finally confirm the applicability at large Ra of the scaling previously proposed by Fu et al. (2013), who highlighted the need of 3D measurements at high- Ra .

As a reference, we also report the mean wavelength obtained in Rayleigh-Bénard-Darcy configuration (De Paoli et al., 2022) (circles in Fig. 2c), where $\hat{\lambda} \sim Ra^{0.19}$ and the flow morphology differs from the present case. This is possibly due to the relationship holding between the response parameter (Nusselt number) and Ra , which is more complex than in one-sided flows (Zhu et al., 2024).

3.1.3 Convective shutdown phase

When a sufficient amount of solute has entered the system, the domain homogenizes and the bulk concentration increases progressively (see Fig. S4c), diminishing the fluid density contrast between the upper boundary and the bulk. As a result, the effective driving force of the flow reduces, as well as the amount of solute entering the system. This mechanism is defined as *shutdown of convection* (Hewitt et al., 2013). In 2D, it has been accurately described by so-called “box models” (Hewitt et al., 2013; Slim, 2014). To model present 3D results, we will employ the approach of Slim (2014), which we observed to better fit the current results. It relies on the approximation of well-mixed bulk (verified also in the 3D case, see Fig. S4c). Therefore, this model is designed to describe well the flow behavior during the late phases, while the accuracy during the transition from constant flux to the shutdown regimes is lower.

Assuming a uniform concentration field far from the upper wall, one can derive an exact form for the evolution of the bulk concentration, which is related to: (a) the critical Rayleigh number (Horton & Rogers Jr, 1945; Lapwood, 1948, $Ra_c = 4\pi^2$), (b) the beginning of the shutdown regime (\hat{t}_{sd}) and (c) a fitting parameter related to the bulk concentration (c_0). Combining this expression of the bulk concentration with definition (10) and integrating Eq. (7) over the volume, we obtain a prediction for the evolution of the shutdown flux:

$$\hat{F}_{sd}(t) = \frac{Ra_{cr}(1 - c_0)^2}{[(1 - c_0)(\hat{t}/Ra - t_{sd}) + Ra_{cr}]^2}. \quad (16)$$

We refer to Slim (2014) for further details on the model’s derivation.

In 2D, we obtain that the best-fitting parameters are $Ra_{cr} = 31.5$, $t_{sd} = 16$ and $c_0 = 0.2716$, analogue to the results reported by Slim (2014). Comparison of the model predictions against the numerical results (not shown here) indicates that Eq. (16) approximates very well the flux also for the present simulations, especially for large Ra and far from the transition to shutdown. Similarly, we found that the model parameters that are suitable to describe the 3D system are $Ra_{cr} = 27.0$, $t_{sd} = 14$ and $c_0 = 0.2697$ (further details on the constraints of these parameters are provided in Sec. 3.2.1). One can observe in Fig. S5 that also in the 3D case the predictions of the model (16) are accurate.

3.2 Volume of solute dissolved

While the flux $\widehat{F}(\widehat{t})$ is representative of the instantaneous flow configuration, determining the cumulative amount of flux dissolved is also crucial, as it allows to estimate, for instance, how long it takes for the system to dissolve a given volume of the solute. In the frame of CO₂ storage, this is key to determine whether or not a formation is safe: if the time taken to dissolve the injected fluid is excessively long, then it is possible that a fracture in the upper low-permeability layer confining the buoyant CO₂ may lead to a leakage to the upper layers before a major proportion of CO₂ has mixed. Here we quantify the amount of solute mixed via the parameter

$$\widehat{M}(\widehat{t}) = \int_0^{\widehat{t}} \widehat{F}(\tau) \, d\tau, \quad (17)$$

and the corresponding quantity in convective units reads $M = \widehat{M}/Ra$. Note that M is also representative of degree of mixing (Jha et al., 2011, $M = 0$ means solute-free, while the volume is fully saturated for $M = 1$). Correspondingly, we have that $0 \leq \widehat{M} \leq Ra$.

The volume dissolved expressed in convective units is reported in Fig. S6(a) as a function of time \widehat{t} (diffusive units). This choice of dimensionless variables allows to distinguish the behavior at different Ra and also to compare directly the evolution of 2D and 3D flows. Provided that the flux in 3D simulations is larger than in the corresponding 2D system (see Fig. 2a), the cumulative amount of solute dissolved is also larger in 3D than in 2D. A small difference may occur at very early times ($\widehat{t} < 2 \times 10^3$), due to an earlier onset of convection in 2D compared to 3D: this is responsible for the slightly larger values of M in 2D than in 3D, e.g., observed in Fig. S6(a) for A1-A3 compared to B1-B3.

In Fig. S6(b) we evaluate the accuracy of the model in describing the 3D results. Integrating Eq. (16) as in (17), we obtain:

$$\widehat{M}_{sd}(t) = \widehat{M}(t_0) + \int_{t_0}^t \widehat{F}_{sd}(\tau) \, d\tau, \quad (18)$$

where we considered as a starting point $t_0 = 14$ and $\widehat{M}(t_0)$, with $\widehat{M}(t_0)$ is computed numerically as in (17). The point $(t_0, \widehat{M}(t_0))$ is marked by a symbol (o) in Fig. S6(b). Choosing the value measured from the simulations as a starting point allows us to evaluate the accuracy of the model in the shutdown phase, which appears to be excellent for all Ra considered. In the following, we will relax this assumption and provide a formulation that is independent of the starting point considered.

3.2.1 Model for the volume dissolved across all phases

We finally provide a model to predict the volume of solute dissolved throughout all the phases of the mixing process. We focus on the high- Ra behavior in which all the regimes are present, and therefore we only consider for the model validation the simulations B5–B10, which we report in Fig. 3(a-b). We split the flow evolution into three main regimes (Slim,

2014), discussed in Sec. 3.1: diffusive, constant flux and shutdown of convection. The unified piecewise model reads:

$$\widehat{M}(\widehat{t}) = \begin{cases} \frac{2\sqrt{\widehat{t}}}{\sqrt{\pi}}, & \text{for } \widehat{t} < \widehat{t}_1 \\ \frac{2\sqrt{\widehat{t}_1}}{\sqrt{\pi}} + \widehat{F}_c(\widehat{t} - \widehat{t}_1), & \text{for } \widehat{t}_1 \leq \widehat{t} < \widehat{t}_2 \\ \frac{2\sqrt{\widehat{t}_1}}{\sqrt{\pi}} + \widehat{F}_c(\widehat{t}_2 - \widehat{t}_1) + \frac{Ra(1-c_0)^2(\widehat{t}/Ra - t_{sd})}{(1-c_0)(\widehat{t}/Ra - t_{sd}) + Ra_{cr}}, & \text{for } \widehat{t} \geq \widehat{t}_2 \end{cases} \quad (19)$$

with $\widehat{t}_1 = 2 \times 10^3$, $\widehat{t}_2 = t_{sd} Ra$ and \widehat{F}_c defined as in Sec. 3.1.2. This simple model is obtained from integration in time of Eqs. (11), (13) and (16) (a summary of the model parameters employed in 2D and 3D is available in Tab. S3). Note that $\widehat{M}(\widehat{t} \rightarrow \infty) = Ra$, assuming that a full saturation is achieved asymptotically. This condition is achieved for

$$c_0 = t_{sd} \widehat{F}_c \quad \text{and} \quad \widehat{t}_1 = \left[2 / \left(\sqrt{\pi} \widehat{F}_c \right) \right]^2, \quad (20)$$

with t_{sd} and \widehat{F}_c measured from the numerical simulations. As a result of these additional constraints, the only fitting parameter is Ra_{cr} .

We observe in Fig. 3(a-b) that the model captures very well the dissolution dynamics during the whole flow evolution. The transition between two regimes is marked by symbols (diamond for \widehat{t}_1 - transition from diffusive to constant flux - and bullets for \widehat{t}_2 - constant flux to shutdown). The predictions of the model are excellent in the short term and also on the long term, see Figs. 3(a) and 3(b), respectively. The availability of such a simple and accurate model is key to deliver long-term predictions on the flow evolution, which will be discussed in Sec. 4.

4 Application to CO₂ sequestration

We employ the model (19) to investigate the dissolution dynamics in terms of cumulative amount of solute dissolved (either volume or mass, since the flow is considered incompressible) over a wide range of times and Ra .

The volume of solute in the system, \widehat{M} , is presented in Fig. 3(c). For better visualization, $\log \widehat{M}$ is shown. At very early times ($t \leq \widehat{t}_1$), \widehat{M} is independent of Ra . Afterwards, Ra determines the dynamics: asymptotically the volume is $\widehat{M} \rightarrow Ra$ and the system saturates. A different interpretation is inferred when looking at Fig. 3(d), where the model results are shown in convective units (t, M). For $Ra \leq 300$, the evolution is time-dependent and the constant flux regime is never achieved. However, for larger Ra , the system becomes independent from Ra , as the shutdown phase is dominant in terms of amount of solute dissolved. The value of M displayed in convective units corresponds also to the fraction of volume saturated with solute. This suggests, for instance, that to saturate a volume corresponding to 50% of the entire domain, $t \approx 30$ is required for nearly all Ra . In contrast, to achieve a 90% saturation, a time $t \approx 250$ is needed.

This model can be employed, for instance, to identify the optimal time and Ra required to dissolve a prescribed amount of solute \widehat{M} . We consider the Sleipner site in the North sea, which we indicated by S_1 . The layer, considered homogeneous and isotropic, has permeability $\kappa = 2.5 \times 10^{-12}$ m² and porosity $\phi = 0.375$. These data as well as the fluid properties later discussed are taken from Neufeld et al. (2010). The density contrast between the CO₂-saturated solution and brine is $\Delta\rho = 10.5$ kg/m³, and the fluid viscosity is $\mu = 5.9 \times 10^{-4}$ Pa s. The diffusion coefficient and the CO₂ solubility are $D = 2 \times 10^{-9}$ m²/s and $C_{\max}^* = 37.8$ kg/m³ (Liu et al., 2024), respectively. This set of parameters fully defines the medium and the fluid properties: we obtain as corresponding scales $\ell^* = 1.718 \times 10^{-3}$ m and $\mathcal{U}^* = 4.364 \times 10^{-7}$ m/s. It follows that, during the constant flux regime, the corresponding average flow cell size near the CO₂-brine interface is $\lambda_c^* \approx 0.5$ m. In Fig. 3(e) we report the dissolved CO₂ mass per unit of surface area as a function of time (t^*) and layer depth

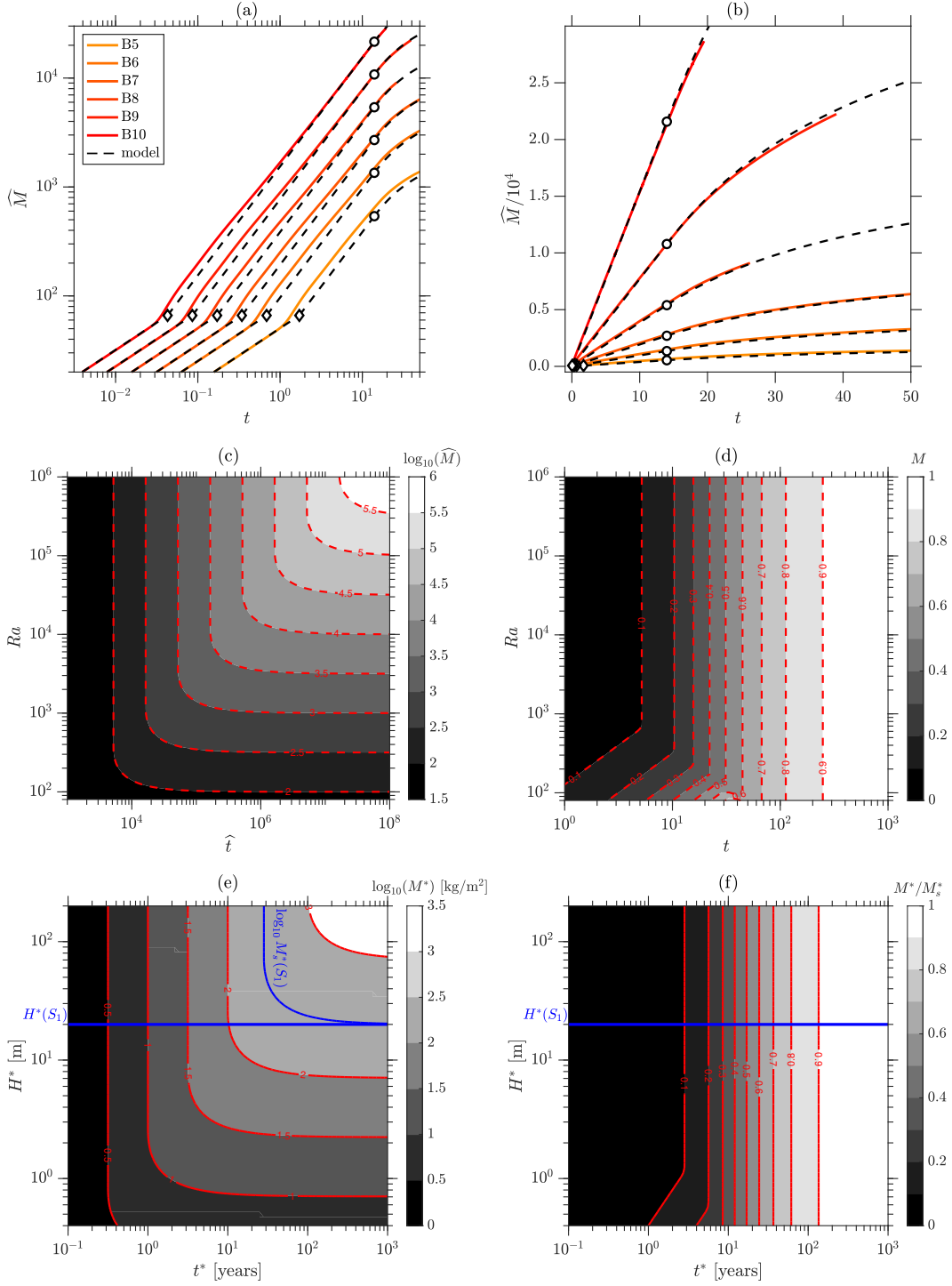


Figure 3. (a-b) Volume of solute dissolved (\widehat{M} , diffusive units) in time (t , convective units). Model (19) is compared against 3D simulations with $Ra \geq 2 \times 10^3$ (B5–B10). Symbols mark the transition between regimes (diamond \widehat{t}_1 , bullet \widehat{t}_2). (c-f) Model predictions for the mass of CO₂ dissolved per unit of surface area. Dimensionless mass is shown as a function of Ra and time, in diffusive (c) and convective units (d). Mass as a function of domain height and time is shown in physical units (e) and normalized with respect to the maximum value, M_s^* (f). Scenario S_1 (Sleipner site, North Sea, see Sec. 4) is indicated in blue.

(H^*). In dimensional form, it is obtained as $M^* = \widehat{M}\phi DC_{\max}^* \tau^* / \ell^*$, with $\tau^* = \phi \ell^* / \mathcal{U}^*$. The maximum amount of solute that can be dissolved is achieved asymptotically and it corresponds to $M_s^* = C_{\max}^* \phi H^*$. For the Sleipner Site $H^*(S_1) = 20$ m (Neufeld et al., 2010) (blue line in Fig. 3e), and we obtain $M_s^*(S_1) = 283.5$ kg/m² and $Ra(S_1) = 1.16 \times 10^4$. Using this model we can also estimate the time required to dissolve a prescribed amount of CO₂: it takes approximately 10 years to mix 100 kg/m², and the same time is required for any formation having height $\geq H^* \geq H^*(S_1)$.

The model presented can be also employed to determine the mixing state within the geological formation. For instance, for the fluid and the medium properties corresponding to S_1 , it is possible to determine the fraction of solute dissolved relative to the maximum, M^*/M_s^* , see Fig. 3(f). Considering the Sleipner Site ($H^*(S_1)$, blue line), it takes < 20 years to achieve a 50% dissolution, but > 100 years to reach 90%, due to the reduction of the strength of convective transport mechanisms during the shutdown phase.

5 Conclusions and outlook

We employed large-scale numerical simulations to study solutal convection in porous media at unprecedented Rayleigh numbers, Ra . We provided, for the first time, a direct comparison of the dynamics of 2D and 3D systems over a wide range of Ra , $10^2 \leq Ra \leq 8 \times 10^4$, and we make this unique dataset freely available (De Paoli et al., 2025). The dissolution dynamics is characterized by the presence of several regimes, from an initial diffusion-dominated phase, to a quasi-steady state (constant flux regime), and finally to the shutdown of convection due to the saturation of the domain. A detailed analysis of the constant flux regime reveals that only for $Ra \geq 5 \times 10^3$ does a constant flux regime occur, and that in 3D the dissolution rate is approximately 13% higher than in 2D. These findings highlight the key role of present 3D simulations, reporting considerably lower values of solute fluxes compared to previous estimates (Pau et al., 2010). The implications of present findings are considerable, since the constant flux is employed as a subgrid parameter in reservoir-scale simulations (MacMinn et al., 2012; Neufeld et al., 2010). We found that for sufficiently high driving ($Ra \geq 5 \times 10^3$), the top boundary develops a hierarchical flow structure that is independent of Ra and drives the formation of large megaplumes in the flow interior. Finally, we proposed a simple model, which we exploit to capture the macroscopic dissolution dynamics during the process of CO₂ storage in the Sleipner Site (North Sea).

The results obtained are relative to homogeneous and isotropic porous media. However, formations identified as possible sequestration sites may be anisotropic (De Paoli et al., 2016; Green & Ennis-King, 2018) and/or heterogeneous (Chen & Yan, 2015; Hidalgo et al., 2022), with possible non-trivial implications on the 3D mixing. In addition, solute redistribution produced by mechanical dispersion (Liang et al., 2018; Wen, Chang, & Hesse, 2018; Tsinober et al., 2022, 2023) may also impact the flow dynamics. Depending on the chemical composition of the geological formation, flow-induced morphology modifications can also influence the dissolution dynamics (Fu et al., 2015; Hidalgo et al., 2015; Miri & Hellevang, 2016). Investigating the role of these additional mechanisms is key to develop safe, reliable and effective CO₂ sequestration strategies (Wang et al., 2022).

Open Research Section

The data of flux presented in this work are available at De Paoli et al. (2025). The data relative to the flux shown in Fig. 2 are available via Pau et al. (2010); Fu et al. (2013); Erfani et al. (2021); De Paoli et al. (2022).

Acknowledgments

This project has received funding from the European Union's Horizon Europe research and innovation programme under the Marie Skłodowska-Curie grant agreement MEDIA

No. 101062123. We acknowledge the EuroHPC Joint Undertaking for awarding the project GEOCOSE number EHPC-REG-2022R03-207 and for granting access to the EuroHPC supercomputer LUMI-C, hosted by the LUMI consortium (Finland).

References

- Chen, C.-Y., & Yan, P.-Y. (2015). A diffuse interface approach to injection-driven flow of different miscibility in heterogeneous porous media. *Phys. Fluids (1994-present)*, *27*(8), 083101.
- De Paoli, M. (2021). Influence of reservoir properties on the dynamics of a migrating current of carbon dioxide. *Phys. Fluids*, *33*(1), 016602.
- De Paoli, M. (2023). Convective mixing in porous media: a review of Darcy, pore-scale and Hele-Shaw studies. *Eur. Phys. J. E*, *46*(12), 129.
- De Paoli, M., Pirozzoli, S., Zonta, F., & Soldati, A. (2022). Strong Rayleigh–Darcy convection regime in three-dimensional porous media. *J. Fluid Mech.*, *943*, A51.
- De Paoli, M., Yerragolam, G. S., Lohse, D., & Verzicco, R. (2024). AFiD-Darcy: A finite difference solver for numerical simulations of convective porous media flows. *Available at SSRN 4995113*.
- De Paoli, M., Zonta, F., Enzenberger, L., Coliban, E., & Pirozzoli, S. (2025, 01). Simulation and modelling of convective mixing of carbon dioxide in geological formations.. Retrieved from <https://doi.org/10.6084/m9.figshare.28175018> doi: 10.6084/m9.figshare.28175018
- De Paoli, M., Zonta, F., & Soldati, A. (2016). Influence of anisotropic permeability on convection in porous media: implications for geological CO₂ sequestration. *Phys. Fluids (1994-present)*, *28*(5), 056601.
- De Paoli, M., Zonta, F., & Soldati, A. (2017). Dissolution in anisotropic porous media: Modelling convection regimes from onset to shutdown. *Phys. Fluids (1994-present)*, *29*(2), 026601.
- De Wit, A. (2004). Miscible density fingering of chemical fronts in porous media: nonlinear simulations. *Phys. Fluids (1994-present)*, *16*(1), 163–175.
- Emami-Meybodi, H. (2017). Stability analysis of dissolution-driven convection in porous media. *Phys. Fluids*, *29*(1), 014102.
- Emami-Meybodi, H., Hassanzadeh, H., Green, C. P., & Ennis-King, J. (2015). Convective dissolution of CO₂ in saline aquifers: Progress in modeling and experiments. *Int. J. Greenh. Gas Con.*, *40*, 238–266.
- Ennis-King, J., Preston, I., & Paterson, L. (2005). Onset of convection in anisotropic porous media subject to a rapid change in boundary conditions. *Phys. Fluids (1994-present)*, *17*(8), 084107.
- Erfani, H., Babaei, M., & Niasar, V. (2021). Dynamics of CO₂ density-driven flow in carbonate aquifers: Effects of dispersion and geochemistry. *Water Resour. Res.*, *57*(4), e2020WR027829.
- Feltham, D. L. (2006). Sea ice is a mushy layer. *Geophysical Research Letters*, *33*(14), L14501. doi: 10.1029/2006GL026290
- Fu, X., Cueto-Felgueroso, L., Bolster, D., & Juanes, R. (2015). Rock dissolution patterns and geochemical shutdown of CO₂-brine-carbonate reactions during convective mixing in porous media. *J. Fluid Mech.*, *764*, 296–315.
- Fu, X., Cueto-Felgueroso, L., & Juanes, R. (2013). Pattern formation and coarsening dynamics in three-dimensional convective mixing in porous media. *Philos. T. R. Soc. A*, *371*(2004), 20120355.
- Gasda, S., Nordbotten, J., & Celia, M. (2011). Vertically averaged approaches for CO₂ migration with solubility trapping. *Water Resour. Res.*, *47*(5).
- Green, C., & Ennis-King, J. (2018). Steady flux regime during convective mixing in three-dimensional heterogeneous porous media. *Fluids*, *3*(3), 58.
- Hesse, M. A. (2008). *Mathematical modeling and multiscale simulation for CO₂ storage in saline aquifers* (Unpublished doctoral dissertation). Department of Energy Resources

- Engineering, Stanford University.
- Hewitt, D. (2020). Vigorous convection in porous media. *Proc. Math. Phys. Eng. Sci.*, *476*(2239), 20200111.
- Hewitt, D., Neufeld, J., & Lister, J. (2013). Convective shutdown in a porous medium at high Rayleigh number. *J. Fluid Mech.*, *719*, 551–586.
- Hewitt, D., Neufeld, J., & Lister, J. (2014). High Rayleigh number convection in a three-dimensional porous medium. *J. Fluid Mech.*, *748*, 879–895.
- Hidalgo, J., Dentz, M., Cabeza, Y., & Carrera, J. (2015). Dissolution patterns and mixing dynamics in unstable reactive flow. *Geophys. Res. Lett.*, *42*(15), 6357–6364.
- Hidalgo, J., MacMinn, C. W., & Juanes, R. (2013). Dynamics of convective dissolution from a migrating current of carbon dioxide. *Adv. Water Resour.*, *62*, 511–519.
- Hidalgo, J., Neuweiler, I., & Dentz, M. (2022). Advective trapping in the flow through composite heterogeneous porous media. *Transp. Porous Med.*, *143*(3), 599–618.
- Horton, C., & Rogers Jr, F. (1945). Convection currents in a porous medium. *Journal of Applied Physics*, *16*(6), 367–370.
- Hu, C., Xu, K., & Yang, Y. (2023). Effects of the geothermal gradient on the convective dissolution in CO₂ sequestration. *J. Fluid Mech.*, *963*, A23.
- Huppert, H., & Neufeld, J. (2014). The fluid mechanics of carbon dioxide sequestration. *Ann. Rev. Fluid Mech.*, *46*, 255–272.
- Imuetinyan, H., Fruton, P., Giraudet, C., & Crococolo, F. (2024). Convective plume spreading in model transparent porous media. *Transp. Porous Media*, 1–22.
- Jha, B., Cueto-Felgueroso, L., & Juanes, R. (2011). Quantifying mixing in viscously unstable porous media flows. *Phys. Rev. E*, *84*(6), 066312.
- Landman, A. J., & Schotting, R. J. (2007). Heat and brine transp. porous media: the Oberbeck-Boussinesq approximation revisited. *Transp. Porous Media*, *70*(3), 355–373.
- Lapwood, E. (1948). Convection of a fluid in a porous medium. *Math. Proc. Camb. Philos. Soc.*, *44*, 508–521.
- Lasser, J., Ernst, M., & Goehring, L. (2021). Stability and dynamics of convection in dry salt lakes. *J. Fluid Mech.*, *917*, A14.
- Lasser, J., Nield, J. M., Ernst, M., Karius, V., Wiggs, G., Threadgold, M., . . . Goehring, L. (2023). Salt polygons and porous media convection. *Phys. Rev. X*, *13*(1), 011025.
- Letelier, J., Ulloa, H., Leyrer, J., & Ortega, J. (2023). Scaling CO₂-brine mixing in permeable media via analogue models. *J. Fluid Mech.*, *962*, A8.
- Liang, Y., Wen, B., Hesse, M., & DiCarlo, D. (2018). Effect of dispersion on solutal convection in porous media. *Geophys. Res. Lett.*, *45*(18), 9690–9698.
- Liu, H., Chen, J., Jin, G., & AlYousef, Z. (2024). Determination of CO₂ convective mixing flux in saline aquifers based on the optimality. *Adv. Geo-Energy Res.*, *13*(2), 89–95.
- Liyanaage, R., Fu, X., Pini, R., & Juanes, R. (2024, Apr). Direct comparison of density-driven convective mixing in a three-dimensional porous medium using experiments and simulation. *Phys. Rev. Fluids*, *9*, 043802.
- MacMinn, C., & Juanes, R. (2013). Buoyant currents arrested by convective dissolution. *Geophys. Res. Lett.*, *40*(10), 2017–2022.
- MacMinn, C., Neufeld, J., Hesse, M., & Huppert, H. (2012). Spreading and convective dissolution of carbon dioxide in vertically confined, horizontal aquifers. *Water Resour. Res.*, *48*(11).
- Miri, R., & Hellevang, H. (2016). Salt precipitation during CO₂ storage—A review. *Int. J. Greenh. Gas Control*, *51*, 136–147.
- Neufeld, J. A., Hesse, M., Riaz, A., Hallworth, M., Tchelepi, H., & Huppert, H. (2010). Convective dissolution of carbon dioxide in saline aquifers. *Geophys. Res. Lett.*, *37*(22).
- Nield, D., & Bejan, A. (2017). *Convection in porous media*. Springer fifth edition.
- Pau, G. S., Bell, J. B., Pruess, K., Almgren, A. S., Lijewski, M. J., & Zhang, K. (2010). High-resolution simulation and characterization of density-driven flow in CO₂ storage in saline aquifers. *Adv. Water Resour.*, *33*(4), 443–455.

- Pirozzoli, S., De Paoli, M., Zonta, F., & Soldati, A. (2021). Towards the ultimate regime in Rayleigh–Darcy convection. *J. Fluid Mech.*, *911*, R4.
- Sin, S., Imai, S., Mahardika, M., Patmonoaji, A., Nasir, M., Susanto, W., ... Suekane, T. (2024). Three-dimensional visualization of Rayleigh–Bénard convection in porous media. *Adv. Water Resour.*, 104666.
- Slim, A. (2014). Solutal-convection regimes in a two-dimensional porous medium. *J. Fluid Mech.*, *741*, 461–491.
- Slim, A., Bandi, M., Miller, J. C., & Mahadevan, L. (2013). Dissolution-driven convection in a Hele–Shaw cell. *Phys. Fluids (1994-present)*, *25*(2), 024101.
- Tsinober, A., Rosenzweig, R., Class, H., Helmig, R., & Shavit, U. (2022). The Role of Mixed Convection and Hydrodynamic Dispersion During CO₂ Dissolution in Saline Aquifers: A Numerical Study. *Water Resour. Res.*, *58*(3).
- Tsinober, A., Shavit, U., & Rosenzweig, R. (2023). Numerical investigation of the influence of hydrodynamic dispersion on solutal natural convection. *Water Resour. Res.*, e2023WR034475.
- Ulloa, H., & Letelier, J. (2022). Energetics and mixing of thermally driven flows in Hele–Shaw cells. *J. Fluid Mech.*, *930*, A16.
- Wang, Y., Vuik, C., & Hajibeygi, H. (2022). Analysis of hydrodynamic trapping interactions during full-cycle injection and migration of co₂ in deep saline aquifers. *Adv. Wat. Res.*, *159*, 104073.
- Wells, A. J., Hitchen, J. R., & Parkinson, J. R. (2019). Mushy-layer growth and convection, with application to sea ice. *Philosophical Transactions of the Royal Society A*, *377*(2146), 20180165.
- Wen, B., Akhbari, D., Zhang, L., & Hesse, M. (2018). Convective carbon dioxide dissolution in a closed porous medium at low pressure. *J. Fluid Mech.*, *854*, 56–87.
- Wen, B., Chang, K., & Hesse, M. (2018). Rayleigh–Darcy convection with hydrodynamic dispersion. *Phys. Rev. Fluids*, *3*(12), 123801.
- Worster, G. (2019). Mushy-layer growth and convection, with application to sea ice. *Philosophical Transactions of the Royal Society A: Mathematical, Physical and Engineering Sciences*, *377*(2146), 20180165. doi: 10.1098/rsta.2018.0165
- Xu, X., Chen, S., & Zhang, D. (2006). Convective stability analysis of the long-term storage of carbon dioxide in deep saline aquifers. *Adv. Water Resour.*, *29*(3), 397–407.
- Zhu, X., Fu, Y., & De Paoli, M. (2024). Transport scaling in porous media convection. *J. Fluid Mech.*, *991*, A4.
- Zonta, F., & Soldati, A. (2018). Stably stratified wall-bounded turbulence. *Appl. Mech. Rev.*, *70*(4), 040801.

Supporting Information for “Simulation and modelling of convective mixing of carbon dioxide in geological formations”

Marco De Paoli^{1,2}, Francesco Zonta³, Lea Enzenberger², Eliza Coliban², and

Sergio Pirozzoli⁴

¹Physics of Fluids Group and Max Planck Center for Complex Fluid Dynamics and J. M. Burgers Centre for Fluid Dynamics,

University of Twente, P.O. Box 217, 7500AE Enschede, The Netherlands

²Institute of Fluid Mechanics and Heat Transfer, TU Wien, 1060 Vienna, Austria

³School of Engineering, Newcastle University, Newcastle upon Tyne NE1 7RU, United Kingdom

⁴Dipartimento di Ingegneria Meccanica e Aerospaziale, Sapienza Università di Roma, 00184 Rome, Italy

Contents of this file

1. **Text S1** and **Table S1**: Numerical details and simulations details.
2. **Text S2** and **Figure S1**: Grid independence tests.
3. **Text S3** and **Figures S2, S3**: Boundary effects/modes restrictions
4. **Figures S4** to **S5**
5. **Tables S2** to **S3**

Additional Supporting Information

1. Captions for **Data Set S1**
2. Caption for **Movie S1**
3. Caption for **Movie S2**

Introduction

This Supporting Information (SI) contains sections providing additional numerical details. In particular, in **Text S1** information about the numerical details is reported and **Table S1** contains the numerical parameters employed for each simulation. Grid independence is discussed in **Text S2** and **Figure S1**. The effect of the boundaries (domain size) on the flux of solute are presented in **Text S3** and **Figures S2-S3**. In addition, **Figures S4** and **S5** are used to provide additional details on the flow dynamics and to validate the model proposed, respectively. A summary of the measurements obtained from the simulations and used to model the flow are provided in **Tables S2-S3**. Finally, the database containing the data obtained (**Data Set S1**) is presented, and a description for the supplementary movies (**Movies S1-S2**) is also provided.

Text S1. Numerical details

The numerical simulations rely on a solver extensively used for Direct Numerical Simulations (DNS) of wall-bounded neutrally-buoyant and unstably-stratified turbulent flows ([Pirozzoli, 2014](#); [Pirozzoli et al., 2017](#)). More recently, it has been employed to resolved Darcy flows in Rayleigh-Bénard configuration ([Pirozzoli et al., 2021](#); [De Paoli et al., 2022](#)). The code, written in the Fortran 90 programming language, was run on LUMI-C (LUMI consortium, Finland) using up to 16,384 cores. All simulations were performed for a total time of $t = 100$ (convective units), but simulations at $Ra \geq 2 \times 10^4$, which were run for shorter time (still long enough to capture the entire flow dynamics) due to the large computational cost (see [Figure 2](#)). For the largest simulations, we used up to 34×10^9 grid points corresponding to 4.2 TB/snapshot. We briefly summarize here the numerical scheme, and we refer to [Pirozzoli et al. \(2021\)](#) and [De Paoli et al. \(2022\)](#) for further details.

The numerical simulations rely on the modified version of a second-order finite-difference incompressible flow solver, based on staggered arrangement of the flow variables (Orlandi, 2000). Eq. (7) is advanced in time by means of a hybrid third-order low-storage Runge-Kutta algorithm, whereby the convective terms are handled explicitly and the diffusive terms are handled implicitly, limited to the vertical direction. A special strategy is used here for the solution of the forced Darcy system (6). By disregarding pressure, at each Runge-Kutta sub-step a provisional velocity field is first determined and is then projected to the space of divergence-free vector functions through a correction step. An efficient direct algorithm, based on Fourier expansions along the periodic directions (Kim & Moin, 1985; Orlandi, 2000), is used here for solving the resulting Poisson equation.

The walls are impermeable to the fluid ($\mathbf{u}^* \cdot \mathbf{n} = 0$, with \mathbf{n} the unit vector perpendicular to the boundary), and slip at the top and bottom boundaries is possible. At the upper boundary the concentration is constant and maximum, namely $C^*(y^* = H^*) = C_{\max}^*$, while at the lower boundary a no-flux condition, $\partial C^*(y^* = 0)/\partial y^* = 0$ (i.e. boundary impermeable to the solute) is applied. Periodicity is considered in the wall-parallel directions. The fluid is initially considered still ($\mathbf{u}^* = 0$) and depleted of solute (i.e. saturated with water only, $C^* = 0$). This configuration is representative of an initial step-like concentration profile.

Table S1. Summary of the simulations performed in this study. We report the Rayleigh number Ra , grid resolution $N_x \times N_y \times N_z$, and domain width in convective (L) and diffusive ($\widehat{L} = L Ra$) units. Note that $L = L_x^*/H^*$ and $L = L_x^*/H^* = L_z^*/H^*$ in 2D and 3D, respectively.

Case	Dim.	Ra	$N_x \times N_y \times N_z$	L	\widehat{L}
A1	2D	1×10^2	$256 \times 16 \times 1$	25	2.5×10^3
A2	2D	2×10^2	$512 \times 24 \times 1$	25	5×10^3
A3	2D	5×10^2	$1280 \times 32 \times 1$	25	1.25×10^4
A4	2D	1×10^3	$2560 \times 48 \times 1$	25	2.5×10^4
A5	2D	2×10^3	$5120 \times 64 \times 1$	25	5×10^4
A6	2D	5×10^3	$5120 \times 128 \times 1$	10	5×10^4
A7	2D	1×10^4	$5120 \times 256 \times 1$	5	5×10^4
A8	2D	2×10^4	$5120 \times 512 \times 1$	2.5	5×10^4
A9	2D	4×10^4	$5120 \times 1024 \times 1$	1.25	5×10^4
A10	2D	8×10^4	$5120 \times 2048 \times 1$	0.625	5×10^4
B1	3D	1×10^2	$64 \times 16 \times 64$	5	5×10^2
B2	3D	2×10^2	$128 \times 24 \times 128$	5	1×10^3
B3	3D	5×10^2	$256 \times 32 \times 256$	5	2.5×10^3
B4	3D	1×10^3	$512 \times 48 \times 512$	5	5×10^3
B5	3D	2×10^3	$1024 \times 64 \times 1024$	5	1×10^4
B6	3D	5×10^3	$1024 \times 128 \times 1024$	2	1×10^4
B7	3D	1×10^4	$1024 \times 256 \times 1024$	1	1×10^4
B8	3D	2×10^4	$1024 \times 512 \times 1024$	0.5	1×10^4
B9	3D	4×10^4	$2048 \times 1024 \times 2048$	0.5	2×10^4
B10	3D	8×10^4	$4096 \times 2048 \times 4096$	0.5	4×10^4

The grid resolution in the horizontal directions is uniform and set according to preliminary grid-independence tests. In particular, a cell size of $\Delta\widehat{x} = \Delta\widehat{z} = 9.766$ is appropriate (further details are provided in Text S2). In the vertical direction, an error function stretching was used to cluster more grid points towards the upper (and lower) boundary layer and thus properly capture the processes that take place there. The resolutions and domain widths considered are indicated in Tab. S1. Given the slightly sub-linear growth of the concentration gradients (Zhu et al., 2024), the number of points in each direction was increased proportionally to Ra . Time stepping is chosen to guarantee a Courant-Friedrichs-Lewy (CFL) number about unity for all

the simulations. Special time step restrictions were implemented for some flow regimes: to fully capture the dynamics during the diffusive regime, the time step is set to $\widehat{\Delta t} = 1$; during the shut-down phase, the velocities are very low and an upper limit for the time-steps is chosen regardless of the CFL-condition. To numerically implement the initial condition discussed in Sec. 2.1, we consider that such a step-like concentration profile allows to determine an analytical self-similar solution of Eq. (7) for the evolution of the concentration field (Slim, 2014; De Paoli et al., 2017):

$$C(x, y, t) = 1 + \operatorname{erf} \left[\frac{(y - 1) Ra}{\sqrt{4t Ra}} \right]. \quad (\text{S1})$$

In order to achieve the same initial condition for all the simulations performed, we initialize the concentration field as in Eq. (S1) with an initial time $t_0 = 250 / Ra$, which is the first instant considered. Finally, a random perturbation a (white noise with amplitude ϵ) is added such that the field at the first instant is defined as:

$$C(x, y, z, t_0) = 1 + \operatorname{erf} \left[\frac{(y - 1) Ra}{\sqrt{4t_0 Ra}} \right] [1 + \epsilon(a - 0.5)]. \quad (\text{S2})$$

The amplitude of the initial perturbation employed to trigger the flow controls the time at which the onset of convection occurs, i.e., it controls the time at which fingers form.

Text S2. Grid independence tests

To investigate the influence of the resolution, a grid sensitivity study has been performed. We considered a squared (cubic) domain, in 2D (3D) at the Rayleigh number $Ra = 10^4$. The grid is uniform in horizontal direction, while in vertical direction points are clustered towards the upper and lower horizontal walls, where small-scale structures and large concentration gradients are

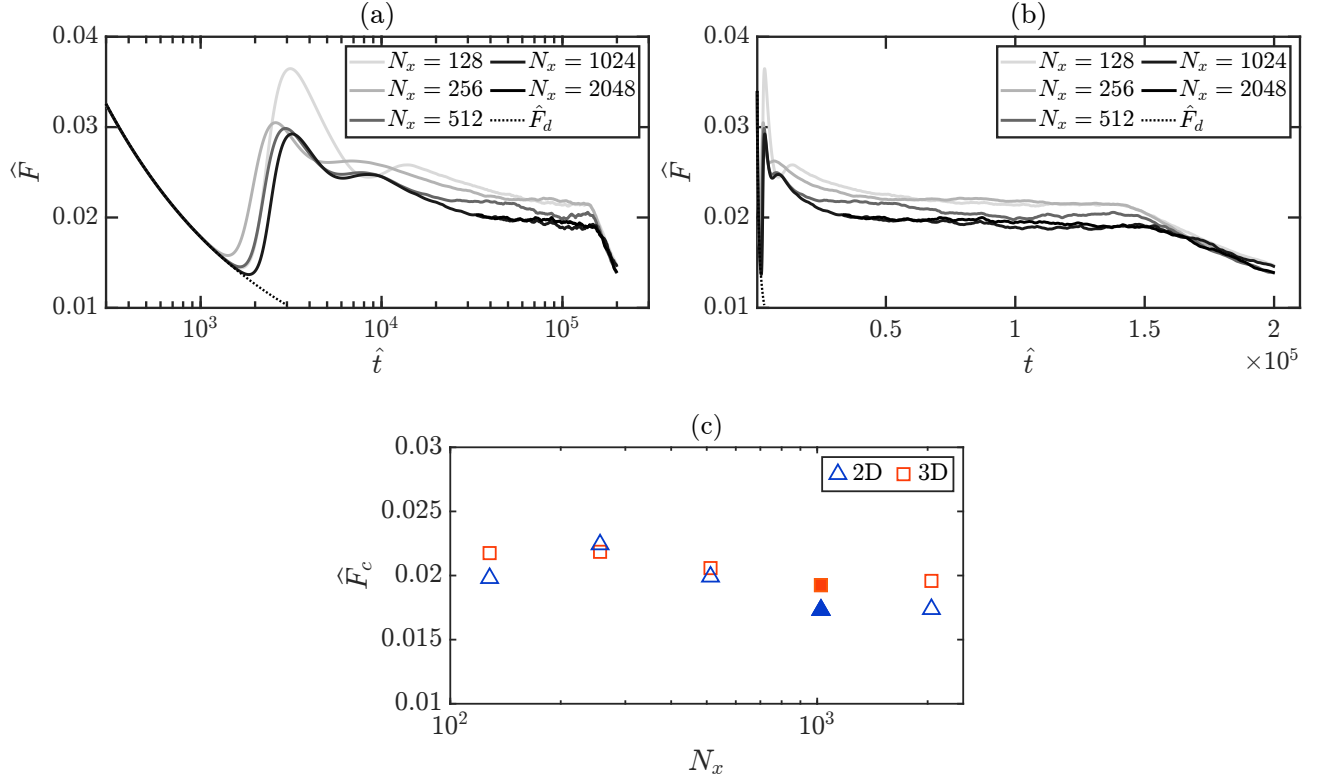


Figure S1. Grid sensitivity for the simulation at $Ra = 10^4$. (a-b) Time-dependent behavior of the dissolution fluxes \hat{F} for the 3D simulations (a - time in logarithmic scale, b - time in linear scale). The number of points used in horizontal direction ($N_x = N_z$) is indicated, as well as the initial diffusive flux (\hat{F}_d , dotted line). (c) Time-averaged dissolution rate \hat{F}_c obtained during the constant flux regime (defined as in the main text), for both 2D (blue triangles) and 3D (red squares) simulations and as a function of the number of nodes. Filled symbols indicated the value employed in the production simulations.

present. The points distribution in the wall-normal direction is obtained using an error function. First we fixed the number of grid points in vertical direction and we investigated the effect of the horizontal resolution, and then we repeated the process for the vertical direction.

In Figs. S1(a,b), we analyzed the instantaneous dissolution flux at the top boundary with $N_y = 256$ and variable $N_x = N_z$. We observe no significant variation for $N_x \geq 1024$. The same trend is observed in the flux averaged during the constant flux regime, \widehat{F}_c , reported in Fig. S1(c) and defined in the main text. In the 2D case, the flux matches the results obtained in previous studies, namely $\widehat{F}_c = 0.017$ (Pau et al., 2010; Slim, 2014; De Paoli et al., 2017; Wen et al., 2018). As a result, the grid resolution in horizontal direction is set to $N_x (= N_z) = 1024$ for $L = 1$ in both 2D and 3D simulations.

The influence of the number of grid points in vertical direction, N_y , has also been considered and the same procedure applied in horizontal direction has been repeated, with N_x (and N_z) fixed and equal to 1024. The analysis of the flux (not reported) indicates that $N_y = 256$ is sufficient. We conclude that a grid size $N_x \times N_y (\times N_z) = 1024 \times 256 (\times 1024)$ is appropriate for $Ra = 1 \times 10^4$ with $L = 1$, corresponding to a horizontal cell size $\Delta\widehat{x} = L Ra / N_x = 9.766$ (in diffusive units), in agreement with previous works (Slim, 2014; Pirozzoli et al., 2021). The number of grid points is set proportionally to Ra and L for all the simulations considered, thus ensuring the same cell size in diffusive units.

Text S3. Boundary effects/modes restrictions

To account for the effects of the periodic boundary conditions and to assess the requirements in terms of domain size, we performed additional simulations in which the horizontal domain width is varied, corresponding to a variation of L . The goal is to identify a domain width that

is sufficiently small, to keep the computational costs accessible, but large enough to capture all the flow features.

The effect of L is quantified again looking at the dissolution rate \widehat{F} , which we report in Fig. S2 for 3D simulations at $Ra = 10^4$. We observe that the aspect ratio has a strong influence on the fluctuations of the dissolution flux, whereas the mean value during the constant flux regime remains nearly unaffected (see Fig. S3). We observe that the constant flux \widehat{F}_c is independent of L within the range of values considered, both in 3D and in 2D simulations (Fig. S3a), although a weak increase is observed for $L = 1/2$ in the 2D case. In contrast, the fluctuations of the flux during the constant flux, quantified by the standard deviation σ , are sensibly affected by the domain size (Fig. S3b). Therefore, we conclude that at $Ra = 10^4$ an aspect ratio $L = 5$ for the 2D case and $L = 1$ for the 3D case is required. The fact that a smaller L is needed for 3D compared to 2D simulations is not surprising: for a fixed L , the additional spatial dimension available in 3D implies a larger area of sampling compared to the 2D case.

The domain width at all Ra considered is varied proportionally, and thus such that $\widehat{L} \geq 10^4$. Only for the low- Ra simulations, in which the constant flux regime is not achieved, the domain width is limited to $L = 5$ (3D) and $L = 25$ (2D). The resolution was also adapted such that the cell size is kept constant (in horizontal direction it reads $\Delta\widehat{x} = \Delta\widehat{z} = 9.766$). Not doing so would result in poor resolution at low Ra and unnecessarily fine resolution at high Ra .

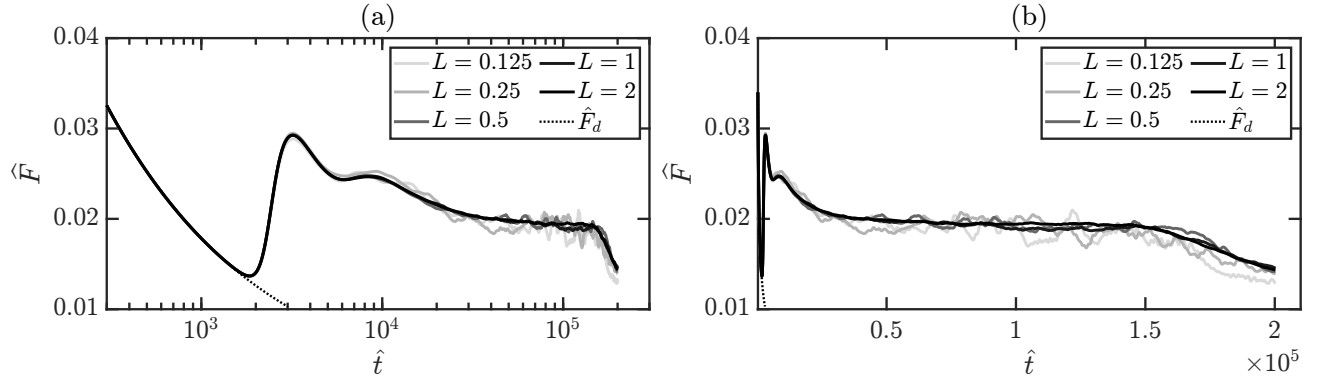


Figure S2. Effect of the horizontal domain size, L , on the time dependent dissolution rate at the top wall in 3D simulations ($Ra = 10^4$, a - time in logarithmic scale, b - time in linear scale).

The initial flux during the diffusive phase (\hat{F}_d , dotted line) is also reported.

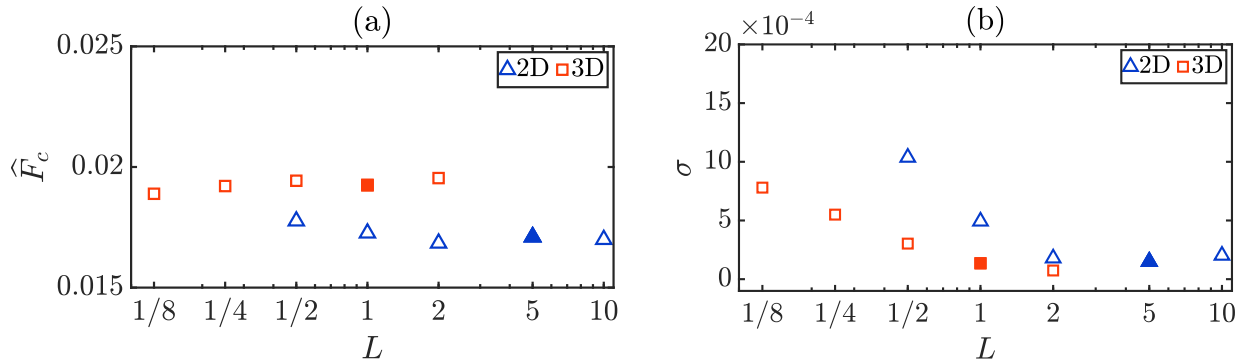


Figure S3. Effect of the horizontal domain size (L) for both 2D and 3D simulations at $Ra = 10^4$ on (a) the average dissolution flux during the constant flux regime, $\langle \hat{F}_c \rangle$, and (b) the mean standard deviation σ of the flux \hat{F} during the constant flux regime. Filled symbols indicate the value of L employed in 2D (blue) and 3D (red) for the production simulations.

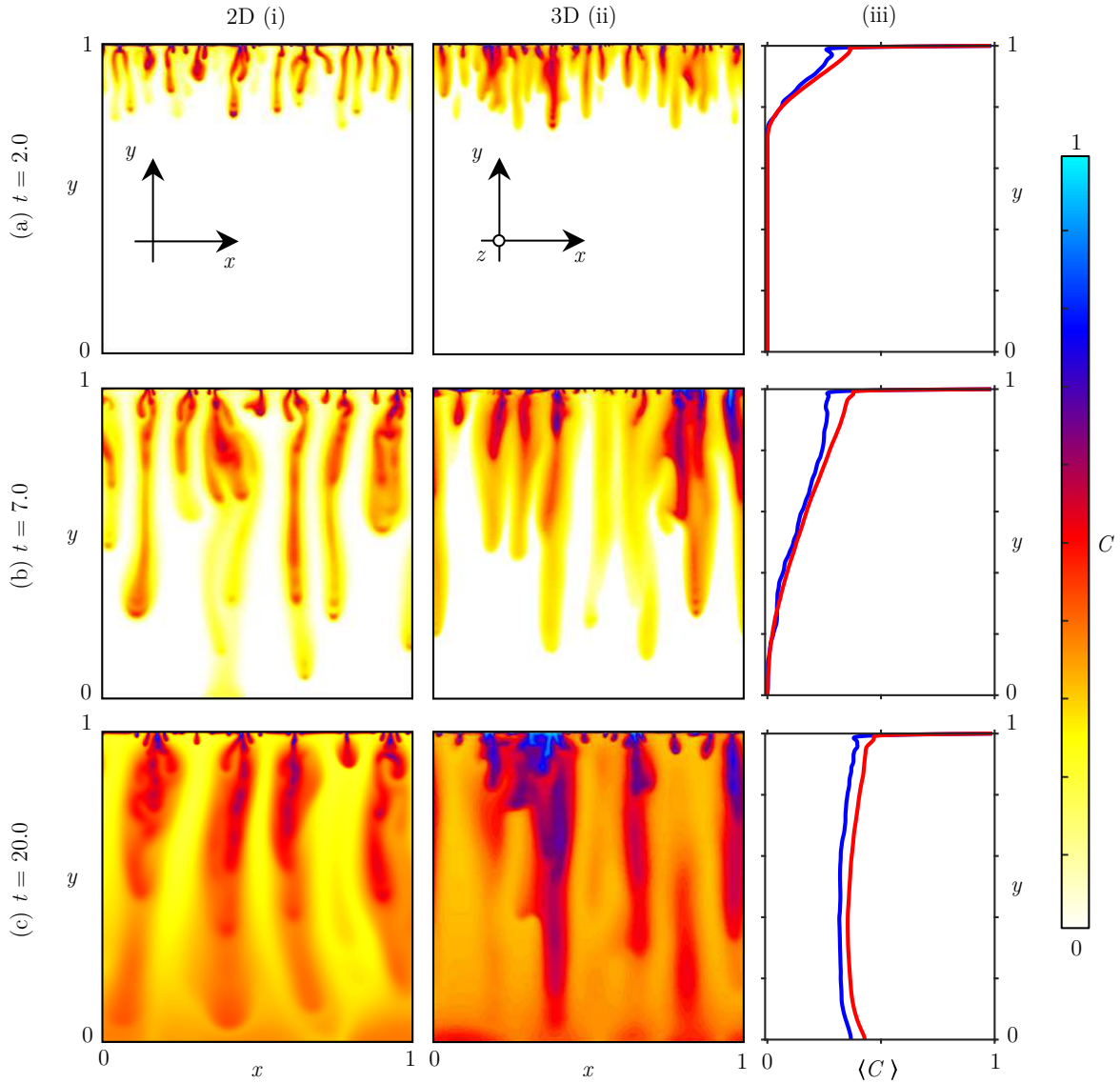


Figure S4. Vertical concentration distributions for $Ra = 10^4$ at different time instants, namely $t = 2$ (panels a), 7 (panels b) and 20 (panels c) for the 2D simulations (left column) and 3D simulations (center column), together with the horizontally-averaged concentration $\langle C \rangle$, shown over the height of the computational domain (right column), where the blue lines represent the 2D data (simulation A7) and the red lines the 3D data (simulation B7).

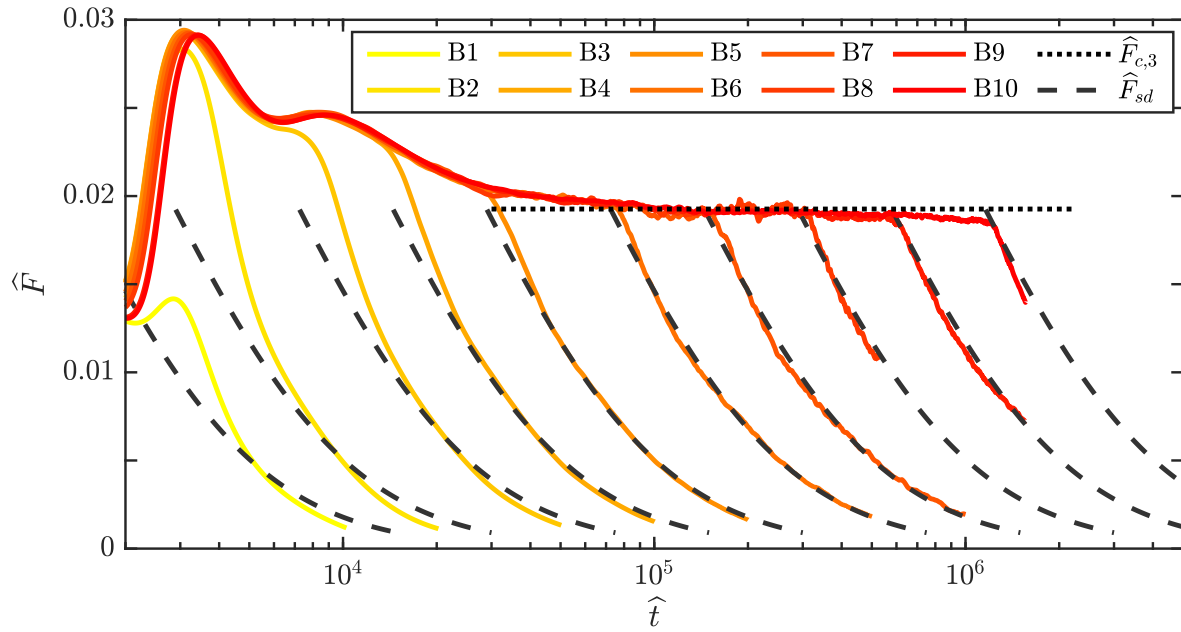


Figure S5. Comparison of the box-model prediction during the shutdown phase against the numerical results in the 3D case. Simulations (solid lines) are compared against the model (\hat{F}_{sd} , (16), dashed lines). The details of the models are presented in Sec. 3.1.3.

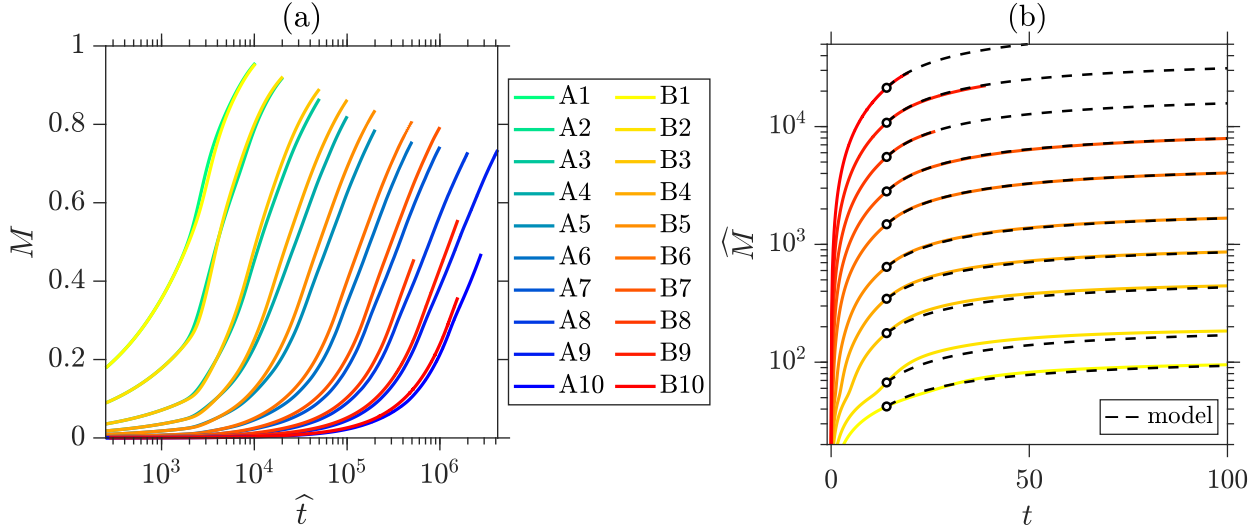


Figure S6. Evolution of the volume of solute dissolved and expressed in (a) convective units M and (b) diffusive units $\widehat{M} = M Ra$, see Eq. (17). In (a), both 2D and 3D simulations are shown (labeled as A# and B#, respectively). In (b), only 3D numerical results are presented together with the model predictions (Eq. (18), dashed lines). The symbols indicates the first instant at which the model is shown (see Sec. 3.2 for further details).

Table S2. Summary of the simulations performed in this study. We report the Rayleigh number Ra , the dissolution flux \widehat{F} and the corresponding standard deviation $\sigma(\widehat{F})$ during the constant flux regime, defined here as $2 \times 10^4 \leq \widehat{t} \leq 16 Ra$ in 2D and $4 \times 10^4 < t < 14 Ra$ in 3D. Finally, the values of the characteristic length scale obtained from the power-averaged mean wave number ($\widehat{\lambda}_c = 1/\widehat{k}$) are also reported. Further numerical details are provided in Tab. S1.

Case	Dim.	Ra	\widehat{F}_c	$\sigma(\widehat{F})$	$\widehat{\lambda}_c$	$\sigma(\widehat{\lambda})$
A1	2D	1×10^2	-	-	-	-
A2	2D	2×10^2	-	-	-	-
A3	2D	5×10^2	-	-	-	-
A4	2D	1×10^3	-	-	-	-
A5	2D	2×10^3	-	-	-	-
A6	2D	5×10^3	0.01672	3.167×10^{-4}	489.3801	32.3486
A7	2D	1×10^4	0.01708	3.949×10^{-4}	457.5535	36.0866
A8	2D	2×10^4	0.01688	5.962×10^{-4}	471.6531	57.4772
A9	2D	4×10^4	0.01715	4.460×10^{-4}	422.7691	34.5794
A10	2D	8×10^4	0.01705	6.835×10^{-4}	434.3080	59.8472
B1	3D	1×10^2	-	-	-	-
B2	3D	2×10^2	-	-	-	-
B3	3D	5×10^2	-	-	-	-
B4	3D	1×10^3	-	-	-	-
B5	3D	2×10^3	-	-	-	-
B6	3D	5×10^3	0.01975	2.125×10^{-4}	253.7446	9.4345
B7	3D	1×10^4	0.01926	3.961×10^{-4}	282.6929	23.0193
B8	3D	2×10^4	0.01933	2.916×10^{-4}	281.7261	22.2302
B9	3D	4×10^4	0.01903	2.679×10^{-4}	288.7920	18.7458
B10	3D	8×10^4	0.01894	2.536×10^{-4}	278.4132	17.7501

Table S3. Summary of parameters employed in 2D and 3D cases. “measurements” indicates the time range used to define the constant flux regime, and over which the quantities \widehat{F}_c and $\widehat{\lambda}_c$ are computed; “model” refers to the parameters used in Eqs. (16) and (19).

Dim.	measurements				model				
	$\widehat{t}_{c,1}$	$\widehat{t}_{c,2}$	\widehat{F}_c	$\widehat{\lambda}_c$	\widehat{t}_1	$\widehat{t}_2 = t_{sd}$	Ra	c_0	Ra_{cr}
2D	2×10^4	$16 Ra$	0.016973	455	4419.7	$16 Ra$		0.2716	31.5
3D	4×10^4	$14 Ra$	0.019264	277	3431.0	$14 Ra$		0.2697	27.0

Data Set S1. A database containing the data of flux for all simulations performed is available (De Paoli et al., 2025). The following quantities are provided:

- Rayleigh-Darcy number: Ra , see Eq. (8) ;
- Time in diffusive units: \hat{t} , see Eq. (9) ;
- Simulation time step in diffusive units: $\Delta\hat{t}$;
- Flux at the top boundary: $\hat{F}(\hat{t})$, see Eq. (10) ;
- Volume of solute dissolved $\hat{M}(\hat{t})$, see Eq. (17) ;

Movie S1. Evolution of simulation A7 ($Ra = 10^4$, only a small portion of the domain in horizontal direction is considered). Top left panel: concentration field. Bottom left panel: Close-up view of the top boundary layer. The process of fingers formation and merging is visible. Center panel: space-time map, $C(x, y = 0.995, t)$, relative to the concentration distribution close to the upper boundary (the height at which the concentration is taken, $y = 0.995$, is indicated by the arrow in the top left panel). The dark blue branches appearing during the constant flux regime ($t < 16$) correspond to the presence of plumes that are persistent in time and space (see Sec. 3.1.2). The beginning of the shutdown phase ($t \approx 16$) is marked by the saturation of the upper boundary layer (blue region in the space time map), and in this regime the plumes are even more persistent. Right panel: Evolution of the dissolution rate at the upper boundary, \hat{F} , as a function of time.

Movie S2. Evolution of the near-wall flow structures for the $Ra = 10^4$ (simulations B7 in Tab. S1). The concentration distribution over a horizontal slice taken at $y = 0.995$ is reported. The convective time, $0 \leq t \leq 85$, indicated in the top left corner, spans over all the regimes. At

this wall-normal location and Ra , fingers appear at $t \approx 1$. They subsequently merge into larger and statistically-steady cells ($4 \leq t \leq 14$). Finally, the driving reduces as a result of the domain saturation, and the near-wall cells dynamics slows progressively down.

References

- De Paoli, M., Pirozzoli, S., Zonta, F., & Soldati, A. (2022). Strong Rayleigh–Darcy convection regime in three-dimensional porous media. *J. Fluid Mech.*, *943*, A51.
- De Paoli, M., Zonta, F., Enzenberger, L., Coliban, E., & Pirozzoli, S. (2025, 01). Simulation and modelling of convective mixing of carbon dioxide in geological formations.. Retrieved from <https://doi.org/10.6084/m9.figshare.28175018> doi: 10.6084/m9.figshare.28175018
- De Paoli, M., Zonta, F., & Soldati, A. (2017). Dissolution in anisotropic porous media: Modelling convection regimes from onset to shutdown. *Phys. Fluids (1994-present)*, *29*(2), 026601.
- Kim, J., & Moin, P. (1985). Application of a fractional-step method to incompressible Navier-Stokes equations. *J. Comput. Phys.*, *59*, 308–323.
- Orlandi, P. (2000). *Fluid flow phenomena: a numerical toolkit*. Kluwer.
- Pau, G. S., Bell, J. B., Pruess, K., Almgren, A. S., Lijewski, M. J., & Zhang, K. (2010). High-resolution simulation and characterization of density-driven flow in CO₂ storage in saline aquifers. *Adv. Water Resour.*, *33*(4), 443–455.
- Pirozzoli, S. (2014). Revisiting the mixing-length hypothesis in the outer part of turbulent wall layers: mean flow and wall friction. *J. Fluid Mech.*, *745*, 378–397.
- Pirozzoli, S., Bernardini, M., Verzicco, R., & Orlandi, P. (2017). Mixed convection in turbulent channels with unstable stratification. *J. Fluid Mech.*, *821*, 482–516.
- Pirozzoli, S., De Paoli, M., Zonta, F., & Soldati, A. (2021). Towards the ultimate regime in

Rayleigh–Darcy convection. *J. Fluid Mech.*, 911, R4.

Slim, A. (2014). Solutal-convection regimes in a two-dimensional porous medium. *J. Fluid Mech.*, 741, 461–491.

Wen, B., Akhbari, D., Zhang, L., & Hesse, M. (2018). Convective carbon dioxide dissolution in a closed porous medium at low pressure. *J. Fluid Mech.*, 854, 56-87.

Zhu, X., Fu, Y., & De Paoli, M. (2024). Transport scaling in porous media convection. *J. Fluid Mech.*, 991, A4.